Software Prototype of IEEE 802.11ad Based Joint Radar Communication Receiver

A THESIS

SUBMITTED IN PARTIAL FULFILLMENT OF THE REQUIREMENTS FOR

THE DEGREE OF

M.Tech

BY
V Sri Sindhu

Electronics and Communication Engineering
(Specialization - Communication and Signal Processing)

INDRAPRASTHA INSTITUTE OF INFORMATION TECHNOLOGY DELHI
NEW DELHI– 110020

September 28, 2022

Certificate

This is to certify that the thesis titled **"Software Prototype of IEEE 802.11ad Based Joint Radar Communication Receiver"** submitted by **V Sri Sindhu** for the partial fulfillment of the requirements of *Master of Technology in Electronics and Communications Engineering* is a record of the bonafide work carried out by her under my guidance and supervision at Indraprastha Institute of Information Technology, Delhi. This work has not been submitted anywhere else for the reward of any other degree.

Dr. Shobha Sundar Ram **Date: September 28, 2022**
Associate Professor
Dr. Sumit J Darak
Associate Professor
Department Of Electronics and Communication
Indraprastha Institute of Information Technology, Delhi

Acknowledgement

It's my pleasure to express my deepest appreciation to my mentors, and friends who supported me immensely during the course of my thesis. My heartfelt gratitude to my supervisors Dr.Shobha Sundar Ram and Dr.Sumit J Darak for the technical guidance, support and motivation during my thesis work, which would not have been possible without their help. I cannot forget the constructive suggestions and inspirational guidance provided by my supervisors that helped me to shape my thesis with the fullest satisfaction. I am extremely thankful to Akanksha Sneh, (Ph.D) and Soumya Jain (M.Tech) for the excellent collaboration during this study. My sincere thanks are also due to IIITD administration for providing me with all the necessary facilities for carrying out the thesis. Lastly, I take this opportunity to thank my family members for all the support extended during my thesis.

Abstract

Rapid beam alignment is required to support high gain millimeter wave (mmW) communication links between a base station (BS) and mobile users (MU). The standard IEEE 802.11ad protocol enables beam alignment at the BS and MU through a lengthy beam training procedure accomplished through additional packet overhead. However, this results in reduced latency and throughput. Auxiliary radar functionality embedded within the communication protocol has been proposed in prior literature to enable rapid beam alignment of communication beams without the requirement of channel overheads. In this thesis, we propose a complete architectural framework of an IEEE 802.11ad based joint radar-communication wireless receiver. We provide a software prototype implementation with receiver design details. The prototype is experimentally evaluated with realistic simulations in free space and Rician propagation conditions and demonstrated to accelerate the beam alignment by a factor of four while reducing the overall bit error rate (BER) resulting in significant improvement in throughput with respect to standard 802.11ad.

Contents

List of Tables

List of Figures

Chapter 1: Introduction

An overarching objective of next generation intelligent transportation systems is to enable vehicle-to-everything (V2X) capabilities along key transport routes to encourage sharing of road and vehicle information pertaining to environmental sensing for reducing road fatalities, and improving driving conditions eventually leading to autonomous driving [1]. Currently, there are three kinds of vehicular communications have been recognised: *dedicated short-range communication services (DSRC)* on IEEE 802.11p based wireless technology [2]; *device-to-device* (D2D) based V2X communications in long-term evolution (LTE), referred as D2D-LTE V2X [3] and *cellular LTE-V2X communications* [4]. All three modes operate in sub-6 GHz spectrum; are restricted to tens of Megabits per second (Mbps) data rates and offer latency of the order of several hundred milliseconds (ms). However, sharing of time-critical high definition three-dimensional environmental maps of congested road conditions between vehicles requires Gigabits per second (Gbps) data rates and ultra-low latency.

The unlicensed spectrum in millimetre wave (mmW) (above 24GHz) offers a viable solution for high bandwidth connected vehicles [5]. Furthermore, there are significant challenges to the practical implementation of mmW transceivers. Due to the high propagation loss at these carrier frequencies, they are meant to operate in short-range line-of-sight (LOS) conditions with highly directional beams realized through beamforming. In high mobility environments, rapid beam training and management result in considerable overhead and significant deterioration of latency [6]. Alternatively, auxiliary sensors such as GPS or standalone radars can aid in beam alignment of the communication systems [7]. However, the deployment of auxiliary sensors increases the cost and complexity in terms of synchronization and data processing as well as poses challenges in terms of interference. In this work, we propose to augment radar functionality within the communications transceiver to enable rapid beam alignment of the communication beams.

Joint radar communication (JRC) systems have been extensively explored over the last several decades over three broad paradigms. The first set of works considered the *coexistence* of radar and communications systems on a common spectrum prompted by RF congestion issues [8–11]. The main objective of these works is to mitigate the mutual interference between the two systems with [9] or without cooperation [10]. These works include communication systems that operate as cognitive radio on federally allocated radar bands [11]; or cognitive radar that operates on communication bands [12]. The second paradigm involves the development and deployment of passive radar receivers with communication transmitters acting as opportunistic illuminators for remote sensing and surveillance applications [13].In the third paradigm, RF front ends - sharing spectrum and hardware - are *co-designed* for both communication and radar sensing functionalities [14, 15]. Here the communication signals are embedded within a traditional radar framework [16, 17] or the radar signals are embedded within the communication uplink or downlink signals [18]. In the other frameworks, either communication or the radar signal is treated as an interference signal or an uncooperative channel [19] and hence the functionality of the

two systems are not fully exploited as in the co-design approach. Our work focuses on the co-design of an IEEE 802.11ad-based dual-functional full duplex transceiver that is capable of joint radar remote sensing and communications.

The IEEE 802.11ad standard specifies the media access control (MAC) and physical layer (PHY) protocols for implementing wireless local area networks through high data rate short range directional communication in the mmW spectrum (57 to 64GHz) [20]. Preliminary studies have demonstrated the effectiveness of JRC implemented upon IEEE 802.11ad (60GHz carrier frequency) for dynamic target tracking [21–23]. In [21], the authors proposed a method of using the IEEE 802.11ad beamforming training protocol for detecting radar targets in the environment. In [24], the authors leveraged the high data rate (1.76GSa/s) and the Golay sequences within the channel estimation fields of the single carrier preamble in the IEEE 802.11ad packet to demonstrate radar ranging with fine range resolution and low sidelobes of a single point target. The authors in [23,25] proposed a modification to the preamble structure to enable Doppler resilient radar ranging of extended dynamic automotive targets. All of these works focused on developing radar signal processing algorithms without complete architectural details of the JRC transceivers and system level performance analysis.

There has been limited work in the prototype, design and experimental demonstrations of co-designed multi-functional transceivers [26–28]. A spatial modulation-based hardware prototype of radar-communication system architecture is proposed in [26], where the transmitted signal consists of individual communications and radar waveforms with index modulation via generalized spatial modulation (GSM). In addition, an array of transmitting antennas has been separated into two sub-arrays, one of which sends the communication signal and the other radar signal. A SIMO JRC architecture that is fully digital was designed on hardware in [27], where the communication signal is received at the target vehicle from the source vehicle and the receiver at the source vehicle receives the radar signals. In [28], a hardware prototype was proposed with modifications to IEEE 802.11ay access points for human sensing and detection. To the best of our knowledge, there is no prior art hardware or software prototype for an end-to-end JRC transceiver.

In this thesis, we propose a complete end-to-end architecture followed by a software implementation of a joint radar-communication framework based on IEEE 802.11 -ad for rapid beam alignment that is capable of half-duplex communication and three-dimensional radar processing along the range, azimuth and Doppler. The contributions of the thesis work can be summarized as follows:

1. Design of software prototype of the IEEE 802.11ad based JRC Receiver architecture realized using Matlab.

2. The proposed software prototype is experimentally evaluated under free space and Rician channel conditions and its communication metrics (throughput and BER) are benchmarked against the standard IEEE 802.11ad protocol.

1.1 Literature Survey

The world's first joint radar communication system was proposed in [29], where some of the pulses transmitted from the missile radars were used to transmit communication information to the space vehicle from the ground.The Linear frequency modulated (LFM) waveform were first utilized in [30] for integration of digital communications and radar.The simultaneous operation of radar and communication systems was achieved in [31] by utilizing the quasi-orthogonality of linear frequency modulated signals having opposite slopes through a single transmitting antenna aperture.The radar and communication transmitters used down chirp and up chirp signals respectively.The probability of detection was measured to be 99% for communication system off as well as for communication system operating at a data rate of 1Mb/s.The best Bit Error Rate (BER) was measured to be 2e-3 for simultaneous operation of radar system and communications.The joint radar communications problem was presented as joint information problem in [19] and various solutions were developed for coexistence of radar and communications for a simple multi access scenario.In the scenario presented in [19],a joint radar communications receiver was considered which can simultaneously decode the received communication signal and estimate the radar target parameters.

A new approach was introduced in [32] to a dual-function radar-communication system. The primary function of the radar system happens in the main lobe that is the target is detected in the main lobe, whereas the sidelobes contain useful information of digital communication signals. At the receiver, each bit is decoded independently from the other bits in the sequence. The radar performs coherent processing as at every radar pulse the same waveform was transmitted. The radar operates in the MIMO mode because of the waveform diversity. It was shown that the process of communication was secure against interference from the other directions. The information delivery is allowed to multiple or single communication directions but it should be outside the main lobe of the radar which contains the target information. The sidelobe level can be modulated using Amplitude Shift Keying (ASK), where the different communication symbols are represented using different powers. The performance of this technique was analysed in respect of the bit error rate.

For the DFRC system, various optimization-based waveform designs were discussed in [33]. The minimization of the downlink multi-user interference (MUI) was the main objective of this paper. Firstly, for the omnidirectional beam pattern by the MIMO radar, the orthogonal waveform design was considered. Weighted optimizations were considered for designing dual-functional waveforms under non-convex power budget constraints to allow a trade-off between the performance of communication and radar. For the transmission to be power efficient both the communication and radar systems need constant modulus signals. Therefore, they considered applying similarity constraints (SC) and constant modulus constraints on the waveform design for more functional optimization. The upper and lower bounds were obtained efficiently by developing the Gradient projection algorithms. The branch-and-bound algorithm was developed to acquire the optimal solutions, which has better performance as compared to the conventional SQR algorithm.

1.2 Notations

Vectors and matrices are indicated with boldface lower and upper case characters respectively, while variables are indicated with regular characters. Radar and communication transmitted signals are indicated by $\mathbf{x}$ and $\mathbf{y}$ respectively while the received signals that have undergone one-way and two-way propagation are shown with $\hat{\mathbf{y}}$ and $\hat{\hat{\mathbf{y}}}$ respectively. Vector superscript $*$ and T denote complex conjugate and transpose respectively. We use the curly braces, $(\cdot)$, to indicate continuous time signals and the square braces, $[\cdot]$, to indicate discrete-time sequences.

Table 1.1: Notations

Description	Symbols
Mobile user transmitter	MU-TX
Mobile user receiver	MU-RX
Base station transmitter	BS-TX
Base station receiver	BS-RX
Communication between BS-TX and MU-RX	Downlink (DL)
Number of OFDM symbols	N_{sym}
Communication between MU-TX and BS-RX	Uplink (UL)
Number of beams at the base station (TRN subfields)	M
Number of beams at mobile user	N
Number of antenna elements at transmitter	N_{TX}
Number of active sub-carriers ($N_{SD} + N_p$)	N_{Tones}
Number of data sub-carriers in each OFDM symbol	N_{SD}
OFDM sampling frequency	fs
Carrier frequency	f_c
Sub-carrier spacing	Δf
Number of pilots in each OFDM symbol	N_p

Chapter 2: System Architecture

To overcome the atmospheric attenuation involved with mmW propagation, directional communication links are necessary. Thus, best beams need to be identified by BS and MU prior to $\mathbf{y}_{\mathrm{DL}}$ and $\mathbf{y}_{\mathrm{UL}}$ communication. The beam alignment procedure is carried out in the standard protocol by utilising in-packet training within the packets [34]. In our proposed architecture, beam alignment was carried out using radar functionality within the BS resulting in a reduction of overall beam alignment time. Standard and the proposed JRC architectures are presented in this section, highlighting the modifications proposed in the former to realize the latter.

2.1 Standard 802.11ad Transceiver Architecture

We begin by providing a brief overview of the packet structure of IEEE 802.11ad PHY layer [20]. The IEEE standard enables transmission of data and header information in three modes namely control, single carrier (SC) and both at sampling frequencies 1.76GHz and 2.64 GHz where later is of Orthogonal Frequency Division Multiplexing mode (OFDM). In our entire analysis, the data is modelled in OFDM mode to ensure high communication throughput and low latency. An 802.11ad PHY packet is constituted by the preamble, header, data and beam refinement protocol (BRF) as shown in Fig.2.1(a).

The preamble of the 802.11ad packet is suitable for channel estimation for communication and radar remote sensing due to its perfect auto correlation properties with zero sidelobes [24]. Further, the header provides necessary control information in order to decode and demodulate the data received. The header is followed by OFDM-modulated data and BRF fields constituted by Golay sequences are added after the data field for enabling beam training between MU and BS. The wireless transceiver architecture for supporting standard 802.11ad communication is presented in Fig.2.2(a). The 802.11ad downlink packets ($\mathbf{y}_{DL}$) generated in the BS-TX are passed through the digital front end (DFE), which consists of a digital-to-analog converter (DAC). Fur-

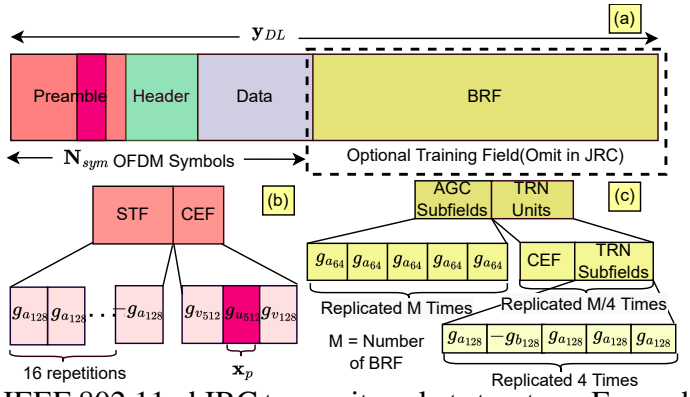

Figure 2.1: (a) IEEE 802.11ad JRC transmit packet structure; Expanded (b) preamble structure and (c) BRF structure.

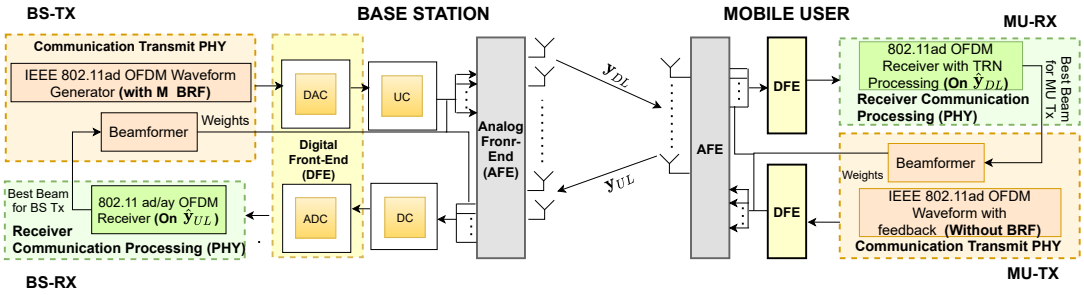

Figure 2.2: Standard IEEE 802.11ad system architecture

ther, the analog signal is modulated with an RF carrier in the analog front end (AFE), amplified and transmitted through a transmit phased antenna array. From here on the beam alignment phase will be referred to as *Stage 1*. During the *Stage 1* the BS-TX transmits a long packet $\mathbf{y}_{\mathrm{DL}}$, where the preamble, header and data are transmitted through a quasi omnidirectional beam. Subsequently, additional M BRF subfields are added at the end of the packet after the data field. Each BRF subfield was steered along the corresponding beam direction by applying suitable antenna weight vectors (AWV) at BS-TX phased array. Further, the data is obtained after down-conversion, digitization and processing of the signal received $\hat{\mathbf{y}}_{DL}$ at the phased array on the MU-RX. The BS repeatedly transmits the $\mathbf{y}_{\mathrm{DL}}$ packet N times and the MU receives each packet sequentially from different beams. The overall complexity involved to estimate the best beam pair is $M \times N$ as M training subfields are received at MU-RX from N beams. After the TRN subfields processing of the N packets at the MU-RX, the best beam pair is estimated from the correlation gains for each beam pair. Beam alignment between BS-TX and MU-RX for $\mathbf{y}_{\mathrm{DL}}$ will provide the requisite information to support the $\mathbf{y}_{\mathrm{UL}}$ communication between MU-TX and BS-RX under the assumption of reciprocity in the propagation environment. This may be due to that the same antennas support both the TX and RX functionalities at both BS and MU in half–duplex mode. The total duration involved in the beam alignment phase includes the duration of N long DL packets each consisting of M TRN subfields, propagation time between the MU and BS and the processing time for communication of the receiver at MU. We enter *Stage 2* with the completion of beam alignment and subsequent communication to the BS regarding the best beam pair. In *Stage 2*, the BS and MU know their best beams for transmission and reception. Now, the BS-TX sends short packets $\mathbf{y}_{\mathrm{DL}}$ without the TRN subfields. The repetition of the beam alignment process depends on the MU mobility and the corresponding signal-to-noise ratio (SNR) estimated at BS and MU. The process of finding the best beam pair returns (*Stage-1*) when the signal-to-noise ratio (SNR) of the received signal at MU falls below a certain threshold value.The steps for beam alignment in *Stage-1* are summarized in Algorithm1.

Algorithm 1 Beam alignment procedure for standard 802.11ad

Step 1: BS-TX sends $n = 1, 2 \cdots, N$ downlink packets, each with M BRF fields. Each m^{th} BRF field is directed along m^{th} pre-determined BS beam.

Step 2: MU-RX receives N packets along $n = 1, 2, \cdots, N$ pre-determined MU beams.

Step 3: The N received packets are processed at MU-RX (RCP) sequentially to determine best beam pair $(\tilde{m}, \tilde{n})$.

Step 4: MU-TX communicates about the $\tilde{m}$ beam to BS through $\mathbf{y}_{UL}$ without BRF field over the $\tilde{n}^{th}$ beam.

Step 5: The BS-RX receives and processes $\hat{\mathbf{y}}_{UL}$ and BS learns about its best beam ,i.e. $\tilde{m}$ for subsequent *Stage-2*. This completes *Stage -1* for the standard architecture.

2.2 Proposed JRC Based 802.11ad architecture

In this thesis, we propose a JRC framework to BS's standard design to minimize the latency caused by the above-discussed beam alignment. This framework is depicted in Fig.2.3. The transmitter at the BS-TX produces both communication (y_{DL}) and radar waveforms ($\mathbf{x}_{\mathrm{p}}$) during the beam alignment *Stage 1*. The optional BRF training fields used in $\mathbf{y}_{\mathrm{DL}}$ for the standard are omitted here resulting in a shorter communication waveform.

The radar waveform was part of the communication packet in the prior art in [23, 35]. However, this results in very short two-way propagation durations (in the order of a few nanoseconds) for short ranges characteristic of automotive environments ($\sim$40 to 200m), which fall within the time-frame of the $\mathbf{y}_{\mathrm{DL}}$ packet (which is of several microseconds). In order to enable the transmission of the downlink packet $\mathbf{y}_{\mathrm{DL}}$ through BS-TX and the reception of the radar reflected signal $\hat{\mathbf{x}}_p$ from the MU at BS-RX, the signal model proposed in the prior art would necessarily require the use of separate sets of antennas or additional hardware at the BS-RX and BS-TX. The architectural choice of embedding radar waveform inside the communication packet as considered in [23,35] increases the cost of the system and also complexity in order to manage the interference introduced by the strong transmission signal received directly at the receiver. Furthermore, the reciprocity in the propagation channels for $\mathbf{y}_{\mathrm{UL}}$ and $\mathbf{y}_{\mathrm{DL}}$ communications would be lost, requiring separate beam alignment procedures for both $\mathbf{y}_{\mathrm{UL}}$ and $\mathbf{y}_{\mathrm{DL}}$. Due to the above-mentioned two reasons, in our proposed architecture we transmit a radar waveform consisting only a portion of the 802.11ad preamble through a quasi-omnidirectional beam. The radar waveform's P pulses, denoted by $\mathbf{x}_{\mathrm{p}}, p = 1 : P$, are transmitted at a pulse repetition interval of T_{PRI}. The same set of antennas can be utilized for both transmission and reception of the radar signal at BS-TX and BS-RX respectively because the radar pulse has a short duty cycle. in comparison to the T_{PRI}.

In the DFE, the radar signals are upconverted from baseband to analog and converted to RF afterwards in AFE. The same AFE and DFE as well as the same phased antenna

array can be utilized for the generation and transmission of both $\mathbf{y}_{\mathrm{DL}}$ and $\mathbf{x}_{\mathrm{p}}$. As a result, there is no increase in the complexity and cost of the system hardware. The transmitted radar signal $\mathbf{x}_{\mathrm{p}}$ scatters at the MU and is reflected back at the BS. At the BS-RX, the received radar signal $\hat{\hat{\mathbf{x}}}_p$ is down-converted at AFE and digitized at the DFE. Further, the signal is passed through a radar-communication decision unit for identifying the reflected returns of radar signal $\hat{\hat{\mathbf{x}}}_p$ from the uplink packet $\hat{\mathbf{y}}_{\mathrm{UL}}$ and the reflected $\hat{\hat{\mathbf{y}}}_{\mathrm{DL}}$ packet. The reflected radar signal $\hat{\hat{\mathbf{x}}}_p$ received at the BS-RX are processed at the radar signal processing unit (RSP). The MU are identified based on their range returns and distinguished from the static clutter based on their Doppler. The location of MU in terms of azimuth and elevation angle is determined in the angular space from radar signal processing. During *Stage 2*, the information from the RSP about the MUs location is given as feedback to the beamformer at BS-TX to enable beam alignment between the BS-TX and BS-RX. The beam alignment at the BS requires a total time combining the radar signal processing time and the duration of the P pulse repetition intervals ($P \times T_{PRI}$). Since the radar signal, $\mathbf{x}_{\mathrm{p}}$ consists of only a portion of the preamble of $\mathbf{y}_{\mathrm{DL}}$, therefore they are much shorter than $\mathbf{y}_{\mathrm{DL}}$.As a result, the beam alignment duration is expected to be considerably lower than the standard. The RSP is implemented only in the BS but not in the MU in our suggested architecture. By taking the complexity and cost into consideration, in our proposed architecture we have implemented digital beamforming at BS-RX and analog beamforming at MU-TX, MU-RX and BS-TX. Therefore the beam alignment procedure at MU will follow the standard protocol. This design choice is made as the BS has a greater number of beams than MU due to the larger number of antennas compared to MU. The beam alignment procedure at MU has been implemented in two versions. In the *Version-1* of the JRC architecture, the MU sends an uplink packet $\mathbf{y}_{\mathrm{UL}}$ with N BRF subfields. The BS-RX determines the best beam for MU by performing a correlation of the BRF subfields. In the next $\mathbf{y}_{\mathrm{DL}}$ packet, the best beam information is transmitted to the MU. Hence, the total time required for the beam alignment at MU includes the duration of one $\mathbf{y}_{\mathrm{UL}}$ with N BRF subfields, propagation delay and the processing times at MU and BS. In the *Version-2* of the JRC architecture, the BS-TX sends N $\mathbf{y}_{\mathrm{DL}}$ packets which are received at the MU-RX along N different beams. The best beam at MU is determined by correlation gains of the preambles of N DL packets received from BS-TX. The duration of *Stage 1* includes the processing time to compute the correlation gains, the propagation delay and the communication processing time. The steps for beam alignment in *Stage-1* for both versions of the JRC architecture are summarized in Algorithm 2. Therefore, for all three architectures, the time required for the beam alignment depends on the packet duration and the signal processing times at BS and MU.

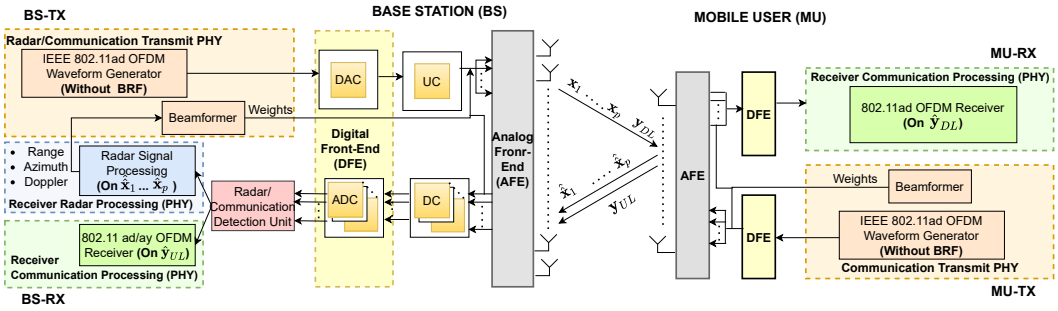

Figure 2.3: Proposed JRC system architecture with beam alignment of BS through radar signal processing and corresponding

---

Algorithm 2 Beam alignment procedure for JRC

Step 1: BS-TX transmits P packets of $\mathbf{x}_p$ with 50% duty cycle through quasi omnidirectional beams which are reflected from the MU and other targets in the environment.

Step 2: The received P packets of $\hat{\hat{x}}_p$ are identified at the radar/comm detection unit and processed at BS-RSP to determine the azimuth of MU (θ_b). Meanwhile, BS-TX transmits quasi-omnidirectional $\mathbf{y}_{DL}$ packets without BRF fields.

Step 3: **Version-1:** The first $\hat{\mathbf{y}}_{DL}$ is received and processed at MU-RX (RCP). Then the MU-TX transmits $\mathbf{y}_{UL}$ with N BRF fields.
Version-2: The first N received $\hat{\mathbf{y}}_{DL}$ packets are processed at MU-RCP and the correlation gains from preamble determines best beam, $\tilde{n}$. The duration of *Stage-1* is based on the greater of the lengths of the two durations - RSP at BS and RCP at MU.

Step 4: **Version-1:** The received $\hat{\mathbf{y}}_{UL}$ is identified at the radar/comm detection unit and processed at BS-RCP when the best beam, $\tilde{n}^{th}$ is determined.

Step 5: **Version-1:** The next $\mathbf{y}_{DL}$ is transmitted without BRF fields along θ_b to MU along with information regarding $\tilde{n}^{th}$ BRF field.

Step 6: **Version-1:** The directional $\hat{\mathbf{y}}_{DL}$ is received and processed at MU-RCP to learn about $\tilde{n}^{th}$ BRF field. This completes *Stage-1*.

Chapter 3: Communication Receiver Processing Block

The aim of the communication receiver is to demodulate and decode the transmitted data correctly. It performs the same tasks as the communication transmitter but in reverse order. The transmitter output propagates from BS-TX to the MU-RX at range r and azimuth θ through the steering vector $\mathbf{u}_\theta^T$. If the MU-RX consists of N_{MU} element ULA, then the received signal at the MU-RX after analog beamforming with antenna weight vector, $\mathbf{w}_{MURX} \in \mathcal{C}^{N_{MU} \times 1}$, is

$$\hat{\mathbf{y}}_{DL_{up}}(t) = \mathbf{w}_{MURX}^T \mathbf{u}_\phi \mathbf{u}_\theta^T \left[\mathbf{Y}_{DL_{up}}(t) * \mathbf{h}^1 \left(\frac{r(t)}{c} \right) \right] + \zeta, \tag{3.1}$$

where $\mathbf{u}_\phi^T = [1 \;\; e^{jkd_{MU} \sin\phi} \;\; \cdots]$ is the steering vector for the BS at ϕ with respect to MU-RX for d_{MU} antenna element spacing, $\mathbf{h}^1(\frac{r(t)}{c})$ is the one-way propagation factor for each MU and ζ is the additive circular-symmetric white Gaussian noise.

Table 3.1: Parameters for the Receiver model

Parameters	Value
Number of data sub-carriers in each OFDM symbol (N_{SD})	336
OFDM Sampling Frequency (T_s)	2.64GHz
Carrier Frequency (f_c)	60GHz
Number of pilots in each OFDM symbol (N_p)	16
FFT operation length (N_{FFT})	512
Number of samples in each OFDM symbol (N_{samp})	640
Number of active sub-carriers (N_{tones})	352
Number of samples in Cyclic Prefix (N_{CP})	128
Sub-carrier spacing (Δf)	5.15MHz
Pilot indices (P_{ind})	[28 48 68 88 108 128 148 168 185 205 225 245 265 285 305 325]

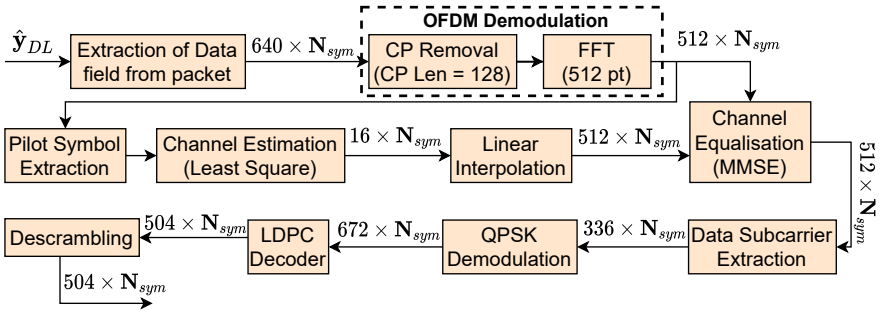

Figure 3.1: Data recovery at communication receiver

The received RF signal is amplified, then down-converted and digitized before it is further processed through the blocks shown in Fig.3.1 to extract data from $\hat{\mathbf{y}}_{DL}$.

3.1 OFDM Demodulation

The cyclic prefix (CP) of 128 samples which was appended at the transmitter to prevent inter-symbol interference (ISI) is removed from each of the received OFDM symbols. After CP removal there are 512 samples in each OFDM symbol. Each OFDM symbol is passed through a 512 point FFT operation to give frequency-domain received symbols. The OFDM demodulated symbols are scaled by the factor as shown in Equation (3.2) after FFT. The active subcarriers (N_{sd} data subcarriers + N_p pilot subcarriers) are extracted. The 16 pilot subcarriers in each symbol are utilized to perform channel estimation.

$$\hat{\mathbf{Y}}_{DL}[k] = \frac{\sqrt{N_{tones}}}{N_{FFT}} \sum_{n=1}^{N_{FFT}} \hat{\mathbf{y}}_{DL}[n] e^{-j2\pi kn/N_{FFT}} \tag{3.2}$$

where N_{tones} is the number of active subcarriers (N_{sd} + N_p) and N_{FFT} is the FFT length.

3.2 Channel Estimation

We considered the IEEE 802.11ad OFDM frame structure with 16 pilot subcarriers in each OFDM symbol. The pilot subcarriers whose values are known at both the transmitter and receiver are inserted at specific indices as mentioned in the document [36]. The frequency domain channel impulse response at the k^{th} pilot subcarrier is estimated using the least square method as shown in Equation (3.3).

$$\hat{\mathbf{H}}[k] = \frac{\hat{\mathbf{Y}}_{DL}[k]}{\mathbf{Y}_{DL}[k]} \tag{3.3}$$

where $\hat{\mathbf{Y}}_{DL}(k)$ and $\mathbf{Y}_{DL}(k)$ are the k^{th} frequency-domain received pilot subcarrier affected by channel and transmitted pilot subcarrier respectively.

3.3 Linear Interpolation

Based on the channel estimation results at the pilot indices, the channel estimates for the N_{SD} data subcarriers are computed using the linear interpolation algorithm. The channel estimate of the l^{th} data subcarrier is given by Equation (3.4). where, P_{ind} is the vector containing the pilot indices and $k = 1, 2...(N_p - 1)$.

$$\hat{\mathbf{H}}[l] = \frac{\hat{\mathbf{H}}[k+1] - \hat{\mathbf{H}}[k]}{\mathbf{P_{ind}}[k+1] - \mathbf{P_{ind}}[k]} (l - \mathbf{P_{ind}}[k]) + \hat{\mathbf{H}}[k] \tag{3.4}$$

3.4 Channel Equalization

The frequency-domain originally transmitted symbols are recovered using a channel equalizer. There are different equalization methods, the most commonly known are

MMSE equalizers [37], zero-forcing (ZF) equalizers, MBER equalizers and maximum likelihood equalizers. The MMSE equalizer used in our receiver design minimizes the mean-square error between the estimated symbols and the originally transmitted symbols as shown in Equation (3.5). After equalization, the estimate of the transmitted data subcarriers for each OFDM symbol is available as shown in Equation (3.6).

$$\mathbf{MSE} = E\{\|\hat{\mathbf{Y}}_{DL} - \hat{\mathbf{Y}}_{DLestimate}\|^2\} \tag{3.5}$$

$$\hat{\mathbf{Y}}_{DLestimate} = \mathbf{H}^*.(\mathbf{H}.\mathbf{H}^* + \frac{\mathbf{1}}{\mathbf{SNR}})^{-1}.\hat{\mathbf{Y}}_{DL} \tag{3.6}$$

3.5 QPSK Demodulation

The algorithm used for the QPSK demodulation in the receiver design is an approximate log-likelihood ratio method. The exact LLR or maximum a posteriori (MAP) decoding algorithm involves a lot of exponentials, logarithms and multiplications therefore it requires a considerable hardware area and computational complexity. The approximate LLR approach was derived by approximating the log-likelihood ratio in the MAP algorithm [38,39]. The approximate LLR algorithm reduces significant computational complexity as it eliminates the use of logarithms and exponentials.The approximate LLR is calculated as shown in Equation (3.7) for each bit. The D_i and D_j represented in Equation (3.8) represent the euclidean distance between the received subcarrier r and the closest constellation point for which the bit value c_k is 0 and 1 respectively. After QPSK demapping we have LLR values of the 672 bits for each OFDM symbol.

$$L[c_k] = \max_{i \in \lambda_{c_k=0}} (D_i) - \max_{j \in \lambda_{c_k=1}} (D_j) \tag{3.7}$$

$$D_i = -\frac{|\ r - s_i\ |^2}{2\sigma^2} \tag{3.8}$$

where $\lambda_{c_k} = 0$ is the set of symbol indices for which $c_k = 0$, and $\lambda_{c_k} = 1$ is the set of symbol indices for which $c_k = 1$,

3.6 LDPC Decoding

The log-likelihood ratio values of the 672 bits after QPSK demodulation are given as input to the LDPC decoder. The LDPC decoder in our receiver design was implemented using the belief propagation algorithm. The parity check matrix H is of dimension P x Q, where P is 168 and Q is 672 i.e. the length of the code-word after demodulation. The H matrix can be expressed using a tanner graph with P check nodes, C_i and Q variable nodes, V_j, where $i = 1, 2, ...P$ and $j = 1, 2, ...Q$. The variable nodes at the beginning of the decoding algorithm are initialized with the LLR values computed during the QPSK demodulation, $m_{V_j->C_i} = x_j$. The estimates for the variable node are calculated at the check nodes and passed as messages $m_{C_i->V_j}$ to the variable nodes (C2V) as shown in Equation (3.9). For the next iterations, only

the extrinsic information is sent back from the variable node to the check node as represented in Equation (3.10). The steps in Equations (3.9)-(3.10) are iterated either till a fixed maximum number of iterations or till all the parity check equations are satisfied. In our case, we are fixing the maximum number of iterations to 12. At the end of all the iterations,LLR_j is the updated estimate of the Log-Likelihood ratio value for the j^{th} transmitted bit. If the LLR_j is less than zero, the hard decision output for the j^{th} bit is 1, otherwise the output is 0.

$$m_{C_i->V_j} = 2\,\mathrm{arctanh}\,(\prod_{j' \in V_j \backslash j} \tanh \frac{m_{V_{j'}->C_i}}{2}) \tag{3.9}$$

$$m_{V_j->C_i} = x_j + \sum_{i' \in C_i \backslash i} m_{C_{i'}->V_j} \tag{3.10}$$

$$LLR_j = x_j + \sum_{i=1}^{P} m_{C_i->V_j} \tag{3.11}$$

3.7 Descrambling

The output of the LDPC decoder LLR is passed through the descrambling block, where a dummy header of 57 bits is added and padded bits are removed and passed through the same scrambling block as the one used in the transmitter. The output after descrambling is the decoded data bits extracted from $\hat{\mathbf{y}}_{DL}$. Similar processing is also done at BS-RX to recover the data transmitted over the uplink $\hat{\mathbf{y}}_{UL}$.

Chapter 4: Simulation Setup

In this section, we describe the simulation setup for evaluating the communication link metrics.

4.1 Target Model

We consider a three-dimensional Cartesian space where xy forms the ground and z is the height axis. We assume that the JRC is located $[0m, 0m, 0m]$ and target motion along two trajectories as shown in Fig.4.1(a) and (b). For the first trajectory, the target starts from an initial position of $[-5m, 10m, 0m]$ and moves over a duration of 1s along the x-axis in a direction tangential to the JRC. In the second case, the target starts at $[-3m, 15m, 0m]$ and moves along the y axis for 1s in a radial direction away from the JRC. We consider a target models/MU to be a simple isotropic point target. For both trajectories, the MU moves with a velocity of 10m/s.

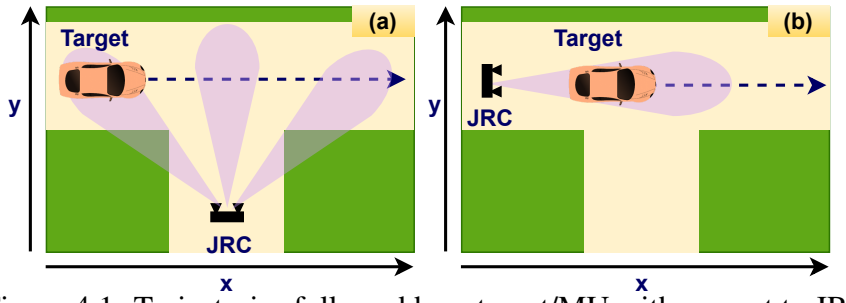

Figure 4.1: Trajectories followed by a target/MU with respect to JRC: (a) tangential motion (b) Radial motion.

4.2 Channel Model

We consider two types of channel models to model the radar ($\mathbf{h}^2$) and communication ($\mathbf{h}^1$) propagation channels. First, we consider an idealistic free space channel model with a direct line-of-sight (LOS) between the BS and MU and no multipath/non-line-of-sight (NLOS). The one-way propagation path between the BS and MU which are r distance apart is given by

$$\mathbf{h}^1\left(\frac{r(t)}{c}\right) = \sqrt{\frac{G_{BS}(\theta)G_{MU}(\phi)L_f(r)\lambda^2}{(4\pi r(t))^2}}\delta\left(t - \frac{r(t)}{c}\right), \tag{4.1}$$

where G_{BS} and G_{MU} are the element patterns of the BS and MU antenna arrays, $L_f(r)$ is the atmospheric attenuation and $\delta(\cdot)$ is the Dirac-delta function. Similarly, the two-way propagation from the BS to the MU and back, for the radar signal is shown as

$$\mathbf{h}^2\left(\frac{2r(t)}{c}\right) = \sqrt{\frac{G_{BS}^2(\theta(t))L_f(2r)\lambda^2}{(4\pi)^3 r^4(t)}}\delta\left(t - \frac{2r(t)}{c}\right). \tag{4.2}$$

Second, we consider the *Rician* fading model which has been popularly used to model outdoor mmW communication [40]. Here, the propagation is characterised by a dominant LOS component and additional NLOS components. The communication signal received at MU-RX shown in (3.1) is modified for the fading channel model as

$$\begin{aligned}\hat{\mathbf{y}}_{DL_{up}}(t) = \mathbf{w}_{MURX}^T \mathbf{u}_\phi \mathbf{u}_\theta^T \left[\mathbf{Y}_{DL_{up}}(t) * \sqrt{\frac{\mathcal{J}}{\mathcal{J}+1}}\mathbf{h}^1\left(\frac{r(t)}{c}\right)\right] \\ + \left[\rho_{nlos}(t) * \sqrt{\frac{1}{\mathcal{J}+1}}\mathbf{h}^1\left(\frac{r(t)}{c}\right)\right] + \zeta,\end{aligned} \tag{4.3}$$

where $\mathcal{J}$ is a Rician factor that is empirically determined for different propagation environments such as rural, urban and suburban [41]. The first term in (4.3) models the direct path in the one-way propagation factor while $\rho_{nlos}(t)$ denotes the signal arising from the multipath that is modelled by an independent and identically distributed complex Gaussian random variable with zero mean and unit variance. The fading channel for two-way propagation of the radar signal $\hat{\hat{\mathbf{X}}}_{p_{up}(t)}$ is modelled by squaring the one-way propagation model in (4.3) for each antenna element at the BS-RX.

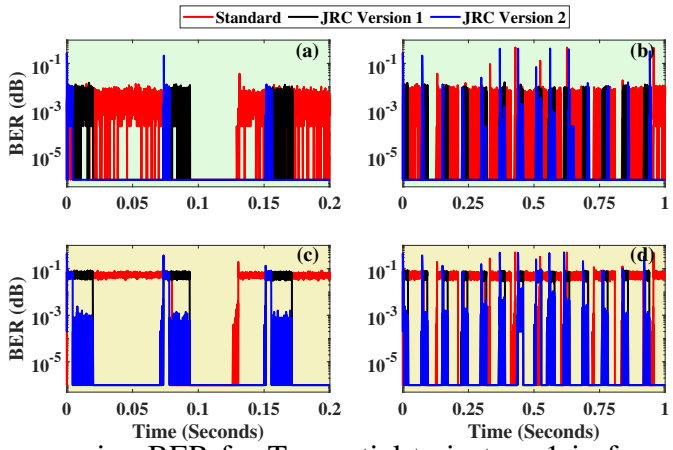

Figure 5.1: Time-varying BER for Tangential trajectory-1 in free space conditions for (a) short duration of 0.2s, (b) long duration of 1s; and Rician space conditions for (c) short duration of 0.2s, (d) long duration of 1s.

Chapter 5: Numerical Results

5.1 Communication metrics

In this section, we report the communication metric - the bit error rate (BER) and throughput - that are calculated on $\hat{\mathbf{y}}_{DL}$ at MU in Fig. 5.1 and Fig. 5.2. The BER is the number of error bits out of the total transmitted data bits and is computed for the two different trajectories of the MU and for both free space and Rician channel conditions. The communication receiver is modeled with a system noise temperature of 290K which gives rise to a mean noise floor of -71.7dBm for a receiver bandwidth of 2.64GHz. As the MU moves along the trajectory, the SNR changes based on the distance between the MU and the BS. We plot the BER over the entire duration of each trajectory.

We first discuss the results for the tangential line trajectory-1 under free space conditions, which are displayed in Fig.5.1(a) and (b). During *Stage-1*, we observe that the BER of standard and both versions of JRC are high and then fall in Fig.5.1(a). This corresponds to the poor BER during *Stage-1* because of the poor link metrics arising from the low gain quasi-omnidirectional beams at the BS and MU. This stage is followed by low BER during *Stage-2* with directional links. The *Stage-1* duration for standard, JRC-*Version-1* and JRC-*Version-2* are approximately 0.08s, 0.03s and 0.02s respectively. Hence, the BER is poor for the standard for a longer duration than the JRC versions. Interestingly, the BER for *Version-1* falls within the same time as *Version-2* even though theoretically the former takes longer to complete the beam alignment. This is because the BS beam is aligned within this interval for both versions and the high gain from the BS's ULA contributes towards lowering the BER even when the beam alignment is not completed at the MU for the first version. Thus, for free space conditions, we realize an improvement in the beam alignment by a factor of four for both the JRC versions when compared to the standard. Due to the nature of the trajectory, the mobile target crosses a narrow beam within a short du-

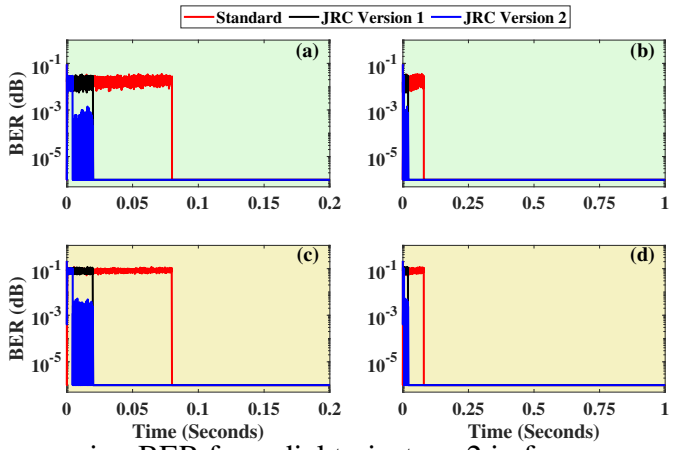

Figure 5.2: Time-varying BER for radial trajectory-2 in free space conditions for (a) short duration of 0.2s, (b) long duration of 1s; and Rician space conditions for (c) short duration of 0.2s, (d) Long duration of 1s.

ration of time and frequent beam alignment is required as shown in Fig.4.1a. When the target is outside of the beam, we observe a deterioration of the BER due to a fall in the SNR in *Stage-2*. This can be observed, for example, between 0.12s and 0.2s in Fig.5.1(b) for standard, and between 0.15s to 0.17s for the JRC versions. Since the standard protocol enables the selection of one of the pre-determined beams while the JRC versions enable directional beams at the recent most angular position of the target, the latter results in better SNR and less frequent beam alignment. The performances of both the standard and the JRC versions deteriorate in Rician conditions resulting in higher BER (as observed in Fig.5.1(c) and (d)) due to strong interference from multipath. Again, we observe that the beam alignment is more rapid for the JRC versions than standard in Fig.5.1c which lowers the overall BER by a factor varying from 8 to 32%.

Next, we discuss the results for the radial trajectory-2 in free space conditions which are displayed in Fig.5.2(a) and (b). Again, the beam alignment duration for the two versions of JRC is much lower than that of the standard in Fig.5.2a. The faster beam alignment (again by a factor of four) at the MU for *Version-2* enables slightly superior performance as evidenced by the results. From Fig.5.2(b), we observe that this trajectory requires less frequent beam alignment between the MU and BS (Fig.4.1b). Once the best beams are identified, the MU remains within the beam for the remaining duration of the motion. The results for the Rician conditions, shown in Fig.5.2 (c) and (d), are much poorer than the free space conditions due to the strong interference from the multipath. Next, we compare the number of packets transmitted during the time interval. As shown in Fig. 5.3, JRC versions allow a higher number of packet transmissions due to smaller packet sizes and fewer beam alignments compared to the standard. The overall communication throughput is calculated based on

$$Throughput = \left(1 - \frac{\sum_{i=1}^{N_p} BER_i}{N_p}\right).\frac{(D)(N_p)}{T_d} \tag{5.1}$$

where, N_p is the number of packets transmitted, T_d is the total duration and D is the number of data bits transmitted in each packet which is kept fixed. The over-

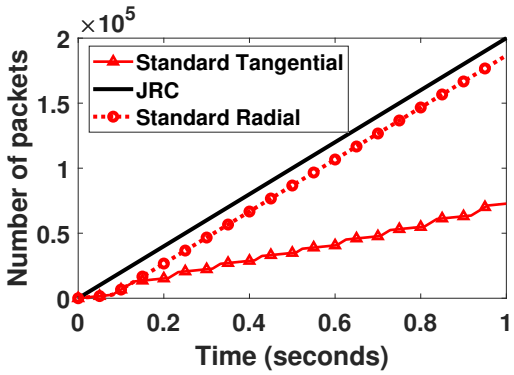

Figure 5.3: Comparison of number of packets communicated over 1 second duration.

all throughput in Gigabits per second (Gbps) for standard, JRC *Version-1* and JRC *Version-2* are presented in Table.5.1.

Table 5.1: Throughput Comparison Of Different Architectures

	Frii's free space			Rician		
Values in Gbps	Standard	JRC *Version-1*	JRC *Version-2*	Standard	JRC *Version-1*	JRC *Version-2*
Trajectory 1 (Translational)	0.336	0.880	0.883	0.329	0.878	0.880
Trajectory 2 (Radial)	0.840	0.883	0.883	0.839	0.881	0.883

The results show that the standard shows a much poorer throughput under both Frii's free space and Rician channel conditions for both trajectories when compared to both versions of the JRC for the first trajectory which required more frequent beam alignments. Even for the second trajectory, the standard has poorer throughput due to the longer beam alignment duration. The throughputs for the two JRC versions are comparable.

Chapter 6: Conclusion

We provide a complete architectural framework of an IEEE 802.11ad-based JRC wireless receiver for enabling mmW communications between BS and fast-moving users. The radar functionality implemented in the JRC provides accurate estimates of the angular positions of the point and extended targets through Doppler, range and azimuth angle. The implementation of radar signal processing at the BS provides an advantage of rapid beam alignment as compared to the beam training procedure which is lengthy for the standard protocol. A complete end-to-end software prototype implementation on MATLAB is provided with receiver design details. For an example case of a system with 32 antennas at the BS and 4 antennas at the MU, we demonstrate the improvement in the communication metrics as the beam alignment timing is improved by a factor of 4 for the JRC with respect to the standard. The main benefit of the JRC is the shorter packet lengths due to the elimination of the additional beam training fields which cause an increase in latency. As a result, more packets are transmitted in a given time for JRC, therefore, increasing the throughput. The overall BER is lower for the JRC due to the precise estimate of the MU's angular position by the radar within the BS.

References

[1] L. Hobert, A. Festag, I. Llatser, L. Altomare, F. Visintainer, and A. Kovacs, "Enhancements of V2X communication in support of cooperative autonomous driving," *IEEE Communications Magazine*, vol. 53, no. 12, pp. 64–70, 2015.

[2] J. B. Kenney, "Dedicated short-range communications (DSRC) standards in the United States," *Proceedings of the IEEE*, vol. 99, no. 7, pp. 1162–1182, 2011.

[3] A. Asadi, Q. Wang, and V. Mancuso, "A survey on device-to-device communication in cellular networks," *IEEE Communications Surveys & Tutorials*, vol. 16, no. 4, pp. 1801–1819, 2014.

[4] P. Wang, B. Di, H. Zhang, K. Bian, and L. Song, "Cellular V2X communications in unlicensed spectrum: Harmonious coexistence with VANET in 5G systems," *IEEE Transactions on Wireless Communications*, vol. 17, no. 8, pp. 5212–5224, 2018.

[5] J. Choi, V. Va, N. Gonzalez-Prelcic, R. Daniels, C. R. Bhat, and R. W. Heath, "Millimeter-wave vehicular communication to support massive automotive sensing," *IEEE Communications Magazine*, vol. 54, no. 12, pp. 160–167, 2016.

[6] C. Liu, M. Li, S. V. Hanly, I. B. Collings, and P. Whiting, "Millimeter wave beam alignment: Large deviations analysis and design insights," *IEEE Journal on Selected Areas in Communications*, vol. 35, no. 7, pp. 1619–1631, 2017.

[7] J. C. Aviles and A. Kouki, "Position-aided mm-wave beam training under NLOS conditions," *IEEE Access*, vol. 4, pp. 8703–8714, 2016.

[8] B. Li and A. P. Petropulu, "Joint transmit designs for coexistence of MIMO wireless communications and sparse sensing radars in clutter," *IEEE Transactions on Aerospace and Electronic Systems*, vol. 53, no. 6, pp. 2846–2864, 2017.

[9] A. F. Martone, K. I. Ranney, K. Sherbondy, K. A. Gallagher, and S. D. Blunt, "Spectrum allocation for noncooperative radar coexistence," *IEEE Transactions on Aerospace and Electronic Systems*, vol. 54, no. 1, pp. 90–105, 2017.

[10] A. Hassanien, M. G. Amin, Y. D. Zhang, and F. Ahmad, "Signaling strategies for dual-function radar communications: An overview," *IEEE Aerospace and Electronic Systems Magazine*, vol. 31, no. 10, pp. 36–45, 2016.

[11] F. Hessar and S. Roy, "Spectrum sharing between a surveillance radar and secondary Wi-Fi networks," *IEEE Transactions on Aerospace and Electronic Systems*, vol. 52, no. 3, pp. 1434–1448, 2016.

[12] K. V. Mishra, Y. C. Eldar, E. Shoshan, M. Namer, and M. Meltsin, "A cognitive sub-nyquist mimo radar prototype," *IEEE Transactions on Aerospace and Electronic Systems*, vol. 56, no. 2, pp. 937–955, 2019.

[13] Y. Zeng, R. Zhang, and T. J. Lim, "Wireless communications with unmanned aerial vehicles: Opportunities and challenges," *IEEE Communications Magazine*, vol. 54, no. 5, pp. 36–42, 2016.

[14] A. Hassanien, M. G. Amin, E. Aboutanios, and B. Himed, "Dual-function radar communication systems: A solution to the spectrum congestion problem," *IEEE Signal Processing Magazine*, vol. 36, no. 5, pp. 115–126, 2019.

[15] S. S. Ram, S. Singhal, and G. Ghatak, "Optimization of network throughput of joint radar communication system using stochastic geometry," *Frontiers in Signal Processing*, vol. 2, 2022.

[16] C. Sahin, J. Jakabosky, P. M. McCormick, J. G. Metcalf, and S. D. Blunt, "A novel approach for embedding communication symbols into physical radar waveforms," in *2017 IEEE Radar Conference (RadarConf)*, pp. 1498–1503, IEEE, 2017.

[17] M. Jamil, H.-J. Zepernick, and M. I. Pettersson, "On integrated radar and communication systems using oppermann sequences," in *MILCOM 2008-2008 IEEE Military Communications Conference*, pp. 1–6, IEEE, 2008.

[18] F. Liu, L. Zhou, C. Masouros, A. Li, W. Luo, and A. Petropulu, "Toward dual-functional radar-communication systems: Optimal waveform design," *IEEE Transactions on Signal Processing*, vol. 66, no. 16, pp. 4264–4279, 2018.

[19] A. R. Chiriyath, B. Paul, and D. W. Bliss, "Radar-communications convergence: Coexistence, cooperation, and co-design," *IEEE Transactions on Cognitive Communications and Networking*, vol. 3, no. 1, pp. 1–12, 2017.

[20] "IEEE Std 802.11™-2016, IEEE standard for information technology—telecommunications and information exchange between systems—local and metropolitan area networks—specific requirements—Part 11: Wireless LAN medium access control," p. 3534, 2016.

[21] E. Grossi, M. Lops, L. Venturino, and A. Zappone, "Opportunistic radar in IEEE 802.11 ad networks," *IEEE Transactions on Signal Processing*, vol. 66, no. 9, pp. 2441–2454, 2018.

[22] P. Kumari, S. A. Vorobyov, and R. W. Heath, "Adaptive virtual waveform design for millimeter-wave joint communication-radar," *IEEE Transactions on Signal Processing*, vol. 68, pp. 715–730, 2019.

[23] G. Duggal, S. Vishwakarma, K. V. Mishra, and S. S. Ram, "Doppler-resilient 802.11 ad-based ultrashort range automotive joint radar-communications system," *IEEE Transactions on Aerospace and Electronic Systems*, vol. 56, no. 5, pp. 4035–4048, 2020.

[24] P. Kumari, J. Choi, N. Gonzalez-Prelcic, and R. W. Heath, "IEEE 802.11ad-based radar: An approach to joint vehicular communication-radar system," *IEEE Transactions on Vehicular Technology*, vol. 67, pp. 3012–3027, Apr. 2018.

[25] G. Duggal, K. V. Mishra, and S. S. Ram, "Micro-doppler and micro-range detection via doppler-resilient 802.11ad-based vehicle-to-pedestrian radar," in *IEEE Radar Conference 2019*, pp. 1–6, 2019.

[26] D. Ma, N. Shlezinger, T. Huang, Y. Shavit, M. Namer, Y. Liu, and Y. C. Eldar, "Spatial modulation for joint radar-communications systems: Design, analysis, and hardware prototype," *IEEE Transactions on Vehicular Technology*, vol. 70, no. 3, pp. 2283–2298, 2021.

[27] P. Kumari, A. Mezghani, and R. W. Heath, "JCR70: A low-complexity millimeter-wave proof-of-concept platform for a fully-digital SIMO joint communication-radar," *IEEE Open Journal of Vehicular Technology*, vol. 2, pp. 218–234, 2021.

[28] J. Pegoraro, J. O. Lacruz, E. Bashirov, M. Rossi, and J. Widmer, "RAPID: Retrofitting IEEE 802.11 ay access points for indoor human detection and sensing," *ArXiv Preprint arXiv:2109.04819*, 2021.

[29] R. M. Mealey, "A method for calculating error probabilities in a radar communication system," *IEEE Transactions on Space Electronics and Telemetry*, vol. 9, no. 2, pp. 37–42, 1963.

[30] M. Roberton and E. Brown, "Integrated radar and communications based on chirped spread-spectrum techniques," in *IEEE MTT-S International Microwave Symposium Digest, 2003*, vol. 1, pp. 611–614, IEEE, 2003.

[31] G. N. Saddik, R. S. Singh, and E. R. Brown, "Ultra-wideband multifunctional communications/radar system," *IEEE Transactions on Microwave Theory and Techniques*, vol. 55, no. 7, pp. 1431–1437, 2007.

[32] A. Hassanien, M. G. Amin, Y. D. Zhang, and F. Ahmad, "Dual-Function Radar-Communications: Information Embedding Using Sidelobe Control and Waveform Diversity," *IEEE Transactions on Signal Processing*, vol. 64, pp. 2168–2181, Apr. 2016.

[33] F. Liu, L. Zhou, C. Masouros, A. Li, W. Luo, and A. Petropulu, "Toward Dual-functional Radar-Communication Systems: Optimal Waveform Design," *IEEE Transactions on Signal Processing*, vol. 66, pp. 4264–4279, Aug. 2018.

[34] Y. M. Tsang, A. S. Poon, and S. Addepalli, "Coding the beams: Improving beamforming training in mmwave communication system," in *2011 IEEE Global Telecommunications Conference-GLOBECOM 2011*, pp. 1–6, IEEE, 2011.

[35] P. Kumari, S. A. Vorobyov, and R. W. Heath, "Adaptive virtual waveform design for millimeter-wave joint communication–radar," *IEEE Transactions on Signal Processing*, vol. 68, pp. 715–730, 2020.

[36] I. . L. S. Committee *et al.*, "Ieee standard for information technology-telecommunication and information exchange between systems-local and metropolitan area networks-specific requirements part11: Wireless lan medium access control (mac) and physical layer (phy) specifications amendment1: Radio resource measurement of wireless lans," *http://standards. ieee. org/getieee802/download/802.11 n-2009. pdf*, 2009.

[37] M. Ibnkahla, *Signal processing for mobile communications handbook*. CRC press, 2004.

[38] A. J. Viterbi, "An intuitive justification and a simplified implementation of the map decoder for convolutional codes," *IEEE Journal on Selected Areas in Communications*, vol. 16, no. 2, pp. 260–264, 1998.

[39] V. B. Olivatto, R. R. Lopes, and E. R. de Lima, "Simplified method for log-likelihood ratio approximation in high-order modulations based on the voronoi decomposition," *IEEE Transactions on Broadcasting*, vol. 63, no. 3, pp. 583–589, 2017.

[40] D. Yan, K. Guan, D. He, B. Ai, Z. Li, J. Kim, H. Chung, and Z. Zhong, "Channel characterization for vehicle-to-infrastructure communications in millimeter-wave band," *IEEE Access*, vol. 8, pp. 42325–42341, 2020.

[41] S. Zhu, T. S. Ghazaany, S. M. Jones, R. A. Abd-Alhameed, J. M. Noras, T. Van Buren, J. Wilson, T. Suggett, and S. Marker, "Probability distribution of rician k-factor in urban, suburban and rural areas using real-world captured data," *IEEE Transactions on Antennas and Propagation*, vol. 62, no. 7, pp. 3835–3839, 2014.